Synchronization characteristics of an array of coupled MEMS limit cycle oscillators

Aditya Bhaskar[a,*], B. Shayak[a], Richard H. Rand[a,b], Alan T. Zehnder[a]

[a] *Sibley School of Mechanical and Aerospace Engineering, Cornell University, Ithaca, New York 14853, USA*
[b] *Department of Mathematics, Cornell University, Ithaca, New York 14853, USA*

Abstract

The dynamics of a proposed microelectromechanical system (MEMS) consisting of an array of limit cycle oscillators (LCOs) are analyzed. The LCOs have dissimilar limit cycle frequencies and are coupled in a nearest-neighbor configuration via electrostatic fringing fields. The emergence of synchrony in the array is outlined for two cases: self-synchronization of the array to a single frequency, and entrainment of the array to an external inertial drive. Numerical analysis is used to study the dependence of synchrony on system parameters such as the coupling strength, detuning in the array, inertial drive strength, and frequency of the inertial drive. It is shown that the route to synchrony is complex due to the formation of frequency clusters. The limit cycle frequency of a single equivalent oscillator, with parameters averaged over the array is used as an estimate for the frequency of locking for the array. This equivalent oscillator is used to approximate the entire array and perturbation methods are applied to it. The perturbation method qualitatively captures the entrainment characteristics of the externally-driven array. This analysis is also used to track the complex sequence of bifurcations that occur as the drive strength changes, and to estimate the threshold drive strength for entrainment.

Keywords: Microelectromechanical system, Limit cycle oscillators, Electrostatic coupling, Self-synchronization, Inertial forcing, Entrainment,

*Corresponding author
Email address: ab2823@cornell.edu (Aditya Bhaskar)

1. Introduction

Microelectromechanical (MEMS) and nanoelectromechanical (NEMS) oscillators are a subclass of micro- and nano-sized devices and consist of a mechanical resonating element driven by a steady energy source. The resonator can be fashioned into different shapes such as doubly clamped beams, nanotubes, dual-disk structures, clamped membranes, and torsional paddles [1, 2, 3, 4, 5]. Notable among these shapes are cantilever and doubly-clamped beams, which have been used in a multitude of frequency-shift based sensing applications such as chemical vapor sensing, mass sensing and force sensing [6, 7, 8], and in various time-keeping devices [9]. The wide range of applications motivates the study of the dynamics of MEMS oscillators that exhibit self-oscillations. Active oscillators which are capable of self-oscillations are to be contrasted with passive resonators which only respond to an external forcing function [10]. Self-oscillations are generated by drawing power from an aperiodic source and maintained via a dissipative mechanism and are described by stable limit cycles in the phase plane for the corresponding dynamical system. In this work, systems that exhibit self-oscillations are termed as *limit cycle oscillators (LCOs)* or *oscillators*.

In a prior work, the dynamics of single MEMS LCO driven by a continuous-wave laser has been analyzed [11]. The oscillator is modeled using a third-order system of coupled nonlinear ordinary differential equations and one of the key findings is the minimum laser power at which the system demonstrates limit cycle oscillations by undergoing a Hopf bifurcation. A single MEMS LCO driven by an external inertial drive has also been studied [12]. Typically, there is a mismatch in the frequency of the inertial drive and that of the LCO. If the strength of the drive is above a threshold, the LCO is entrained by the inertial drive.

LCOs can also interact with each other via coupling fields to form networks of different topologies. Oscillator networks can be engineered, but they are

also found in nature in myriad forms, for example in intestinal muscles, in the circadian rhythm of the human body and sleep-wake cycle, and in socially-synchronized organism colonies like that of fruit flies and honeybees [13, 14, 15]. Further, even simple networks of oscillators can show complex dynamical behavior [16]. This gives us a broader context to study the behavior of oscillator networks. When MEMS LCOs are fabricated, they inadvertently have variable dimensions due to manufacturing limitations and such defects can alter the capabilities of the oscillator to act as high-resolution sensors or stable time-keeping devices. To circumvent this limitation, the device can be built as a network of two or more LCOs and coupled using different methods like mechanical linkages, electrostatic fringing fields, optical radiation fields, and resistors [17, 18, 19, 20]. A network with nearest-neighbor coupling is the focus of this work and such a network is termed an *array*.

In an array of MEMS LCOs, the oscillators typically have different lengths and hence different limit cycle frequencies. Such an array is said to be *frequency-detuned* or *detuned*. An interesting feature of a detuned array of LCOs is the emergence of synchronization. In the presence of sufficient coupling, the dissimilar LCOs interact amongst themselves and show steady oscillations at a single frequency, and the network shows lower phase noise [21] and higher frequency stability [22]. Such a system is said to be *self-synchronized* and the common frequency of all the LCOs is called the *locking frequency*. When such an array is driven externally by an inertial forcing function, it is possible for all the LCOs to oscillate at the frequency of the drive. This is termed as *frequency-entrainment* or *entrainment* to the drive. If the oscillators are not synchronized, they are said to be in a state of *drift*.

In this work, we study the dynamics of an array of eight detuned, electrostatically coupled and laser-driven MEMS LCOs. The physical system is described in detail in Sec. 2. The mathematical model used to describe the system and the numerical methods used to solve the model are discussed in Sec. 3. In Sec. 4, we use these numerical methods to analyze the dynamics of the array of LCOs. Self-synchronization and its onset for different parameter values are studied.

A method to estimate the locking frequency is introduced, which allows us to approximate a self-synchronized array of LCOs using a single equivalent LCO. The response of the array to an external inertial drive is detailed in Sec. 5. The entrainment of all oscillators in the array to the drive is studied using perturbation theory applied to the equivalent oscillator. The method allows us to calculate the threshold drive strength for entrainment and reveals a sequence of bifurcations that the oscillator undergoes en route to entrainment.

2. Description of the physical system

A schematic of the device setup is shown in Fig. 1. The MEMS LCO array envisioned here consists of eight beams, made of silicon, with lengths in the order of tens of micrometers and thicknesses in the order of hundreds of nanometers. The lengths of the beams in the array are dissimilar, either due to unavoidable fabrication imperfections or due to deliberate design choice, and hence the array is detuned. The detuning increases with an increase in the variation in the lengths of the beams. The beams are doubly clamped to the silicon dioxide layer underneath and the silicon dioxide layer itself is supported by a thick silicon handle. The entire device can be fabricated using photolithography and etching on a silicon-on-insulator (SOI) wafer. The silicon beams are supplied with energy using an external continuous-wave laser beam focused at their center. The silicon beams absorb part of the incident laser light and transmit part of it towards the substrate. The substrate then reflects the laser back to the beams which reabsorb the energy. The absorption of the laser light causes thermal stresses to develop in the beams, causing them to bend in the out-of-plane direction. Since the thickness of the beams is of the order of the wavelength of the light, the motion of the beams in the laser field influences the amount of light being absorbed, resulting in opto-thermal feedback. With sufficient laser power this feedback can lead to limit cycle oscillations of the beams [11].

Furthermore, the beams are alternately kept at a fixed non-zero voltage and at ground voltage. This scheme causes electrostatic fringing fields to develop

between the beams and the interactions between neighboring pairs are significant [23, 18]. Due to the presence of the fringing fields, each pair of neighboring beams acts as a capacitor with the attractive force between them changing with the out-of-plane displacement of the beams [24, 25]. The coupling strength can be increased by increasing the voltage applied to the alternate beams. Thus, an array of LCOs is envisioned with nearest-neighbor electrostatic coupling. The entire MEMS device is bonded to a piezoelectric disk which can act as a shaker and provide inertial forcing to the LCO array [26]. The forcing function is typically modelled using a sinusoidal function and the two key parameters that determine the effect of the drive on the array are the *inertial drive strength*, and the *inertial drive frequency*.

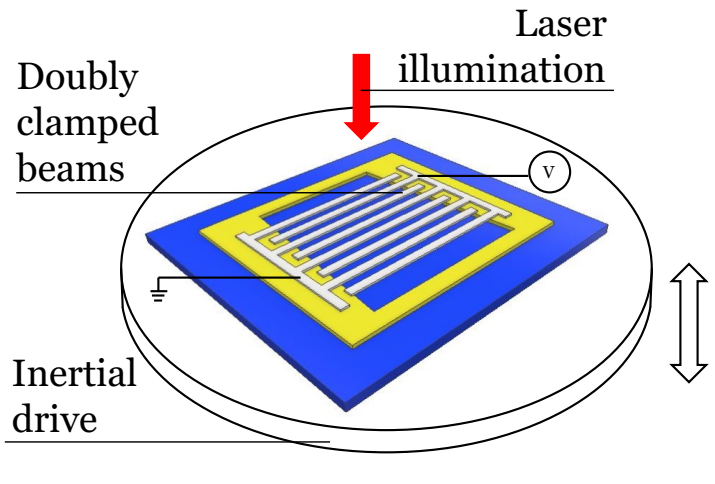

Figure 1: Schematic of a detuned array of eight MEMS LCOs coupled via electrostatic fringing fields. A laser beam of sufficient power, focused at the center of the oscillators, drives them to limit cycle oscillations at different frequencies. In addition, the MEMS device is mounted on a piezoelectric disk which can provide inertial forcing.

3. Mathematical model and numerical methods

The mathematical model describing the dynamics of an array of $n > 2$ detuned, coupled MEMS LCOs, is obtained by extending the model for a pair of coupled MEMS LCOs [27], and is given by Eqs. 1-4.

$$\ddot{z}_1 + \frac{\dot{z}_1}{Q} + \kappa_1(1 + CT_1)z_1 + \beta z_1^3 + \frac{V^2(z_1 - z_2)}{1 + |z_1 - z_2|^p} \dots$$

$$\dots = DT_1 + E\sin(\omega_d t), \tag{1}$$

$$\ddot{z}_i + \frac{\dot{z}_i}{Q} + \kappa_i(1 + CT_i)z_i + \beta z_i^3 + \frac{V^2(z_i - z_{i+1})}{1 + |z_i - z_{i+1}|^p} + \dots$$

$$\dots + \frac{V^2(z_i - z_{i-1})}{1 + |z_i - z_{i-1}|^p} = DT_i + E\sin(\omega_d t), \tag{2}$$

$$\ddot{z}_n + \frac{\dot{z}_n}{Q} + \kappa_n(1 + CT_n)z_n + \beta z_n^3 + \dots$$

$$\dots + \frac{V^2(z_n - z_{n-1})}{1 + |z_n - z_{n-1}|^p} = DT_n + E\sin(\omega_d t), \tag{3}$$

$$\dot{T}_i = -BT_i + HP_{\text{laser}}[\alpha + \gamma \sin^2(2\pi(z_i - \bar{z}))]. \tag{4}$$

The model describes the limit cycle oscillations of the MEMS LCOs using lumped variables, z_i: the out-of-plane displacement of the center of the i^{th} beam normalized by the wavelength of light, and T_i: the average temperature of the i^{th} beam. Q represents the quality factor of the oscillator and is identical for all the LCOs in the array. κ_i is the detuning parameter for the i^{th} oscillator. The detuning parameter for the first oscillator in the array, κ_1, is fixed at unity, and this oscillator acts as the frequency reference. The average of all the detuning parameters in the array, i.e. $\bar{\kappa} = \Sigma\kappa_i/n$, is termed as the average detuning parameter. In this work, the detuning parameters, κ_i, are evenly spaced, and in terms of the average detuning parameter, they vary from 1 to $2\bar{\kappa} - 1$. The farther the average detuning parameter is from unity the more heterogeneous, or detuned, the array is. C is the thermal coefficient for linear stiffness and controls the change in the linear stiffness of the oscillator with change in its average temperature. β is the cubic stiffness of the oscillator. V is the voltage difference between neighboring oscillators and it is used to change the coupling strength in the array. Every neighboring pair has the same voltage difference and hence this parameter is the same in each coupling term in the network. It should be noted that the beams at the end of the array are coupled only to one

Parameter	Value	Units
Q	1240	arb. units
C	0.02	1/K
β	15.5	arb. units
p	2.4	arb. units
D	2.84×10^{-3}	1/K
B	0.112	arb. units
H	6780	K/W
α	0.035	arb. units
γ	0.011	arb. units
$\bar{z}$	0.18	arb. units

Table 1: Values of normalized fixed parameters used in the numerical calculations.

neighboring oscillator while the beams in the interior are coupled to oscillators on either side. This arrangement is reflected in the nature of the coupling terms in Eqs. 1-3. p is a fitting parameter used which introduces nonlinearity in the coupling term [28]. D is the static displacement per unit change in temperature. B and H are thermal constants. P_{laser} is the continuous-wave laser power and represents the input energy fed into this system. A threshold value of laser power is required to drive the silicon beams to limit cycle oscillations [11]. For all calculations in Secs. 4 and 5.1, the laser power is fixed at $P_{\text{laser}} = 2 \times 10^{-3}$ W. α is a parameter representing the minimum absorption, γ is the contrast in absorption and $\bar{z}$ is the equilibrium position of the oscillator with respect to the absorption curve. If the array is externally driven by a piezoelectric disk, the inertial drive strength is given by E, and the inertial drive frequency by ω_d. The values of the constant parameters used in the numerical simulations are given in Tab. 1 and have been obtained from previous work [29]. In Tab. 1, the units for non-dimensionalized parameters are taken to arbitrary units (arb. units).

For performing the numerical study, the system of Eqs. 1-4 is numerically integrated using the odeint function from the Python scipy.integrate sub-package. Starting with appropriate initial conditions, the system is solved for a total time of $50Q$; enough time for the LCOs to reach steady-state limit cycle motion for calculations in Sec. 4. The solutions for the displacement of the oscillators, $z_i(t)$,

are sampled at 10 samples per unit time. The Fast Fourier transform (FFT) of 2^{16} samples from the tail of the displacement time series is computed with a frequency resolution approximately equal to 1.5×10^{-4}. The Fourier frequency corresponding to the maximum amplitude in the magnitude spectrum for an oscillator is assigned as its limit cycle frequency. For a single reference oscillator with $\kappa = 1$, the limit cycle frequency is calculated to be 1.173. Two or more oscillators are said to be self-synchronized if the frequencies, thus calculated, agree up to three decimal places. If the numerically calculated oscillator frequency is the same as that of the drive, up to three decimal places, then the oscillator is said to be entrained.

4. Self-synchronization in an array of coupled oscillators

4.1. Dependence on frequency detuning and coupling strength

The numerical procedure described in Sec. 3 is used in a parametric sweep of 101 equally spaced values of the average detuning parameter, $\bar{\kappa} \in [0.65, 1.35]$ and 101 equally spaced values of the coupling strength, $V^2 \in [0, 0.04]$. The computation was carried out using parallel computing with jobs distributed among 28 cores. In this case, there is no external inertial forcing in the system and thus $E = 0$. For each combination of detuning and coupling strength, the calculation is started with zero initial conditions and the limit cycle frequencies of the LCOs in the array are computed and compared for synchronization. In this parameter space, the maximum number of LCOs locked to a frequency, or the size of the largest frequency-locked cluster, is determined and plotted in Fig. 2. The parameter space has eight nested tongue-like regions, all centered at $\bar{\kappa} = 1$; the detuning value at which no coupling is needed to synchronize the array, since all the oscillators are identical. As the average detuning parameter of the array deviates from unity the coupling strength required to synchronize a certain number of oscillators increases. Also, for the same level of detuning in the array, higher coupling strengths are required to form larger frequency-locked clusters. Tongue-like regions in the frequency detuning vs. coupling strength

parameter space are characteristic of self-synchronizing networks of LCOs [30] and are referred to as *Arnold tongues* [31, 32]. For the MEMS LCO array, each Arnold tongue corresponds to a region of frequency-locked clusters of a certain size. The boundaries of the tongue are of significance because a small change in the detuning or coupling strength is enough to move the system from one tongue to another, a property that could be exploited in sensing applications. For this system, the boundaries of the tongues are indistinct, and this suggests that the synchronization may depend on other factors like initial conditions. This is further explored in Sec. 4.2. For time-keeping applications a single frequency would be desired and the innermost tongue in Fig. 2 gives the parameter values for achieving this.

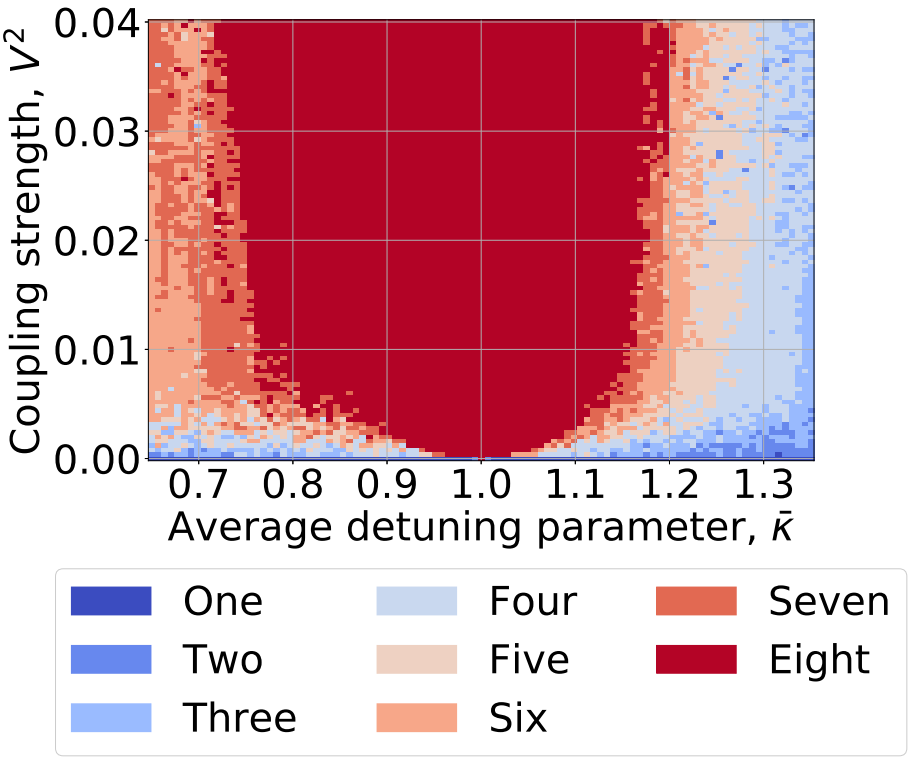

Figure 2: The size of the largest frequency-locked cluster in an array of eight coupled LCOs, plotted in the detuning vs. coupling strength parameter space. The calculations are started with zero initial conditions. A structure with nested Arnold tongues and indistinct boundaries is observed and all the tongues are centered at $\bar{\kappa} = 1$.

Increasing the coupling strength from a zero value, in a system with fixed detuning, and mapping the frequencies of the oscillator reveals the complex cluster states that exist en route to complete self-synchronization. Such a plot is shown in Fig. 3 for detuning $\bar{\kappa} = 1.168$. In this parametric sweep, the coupling strength, V^2, takes 101 equally spaced values in the range $[0, 0.04]$. The limit cycle frequency for each LCO is shown using a color map. For zero coupling, the limit cycle frequencies are $(1.173, 1.19, 1.206, 1.221, 1.238, 1.254, 1.27, 1.286)$, and are all distinct because the array is detuned. As the coupling strength is increased, frequency-locked clusters form in the system, but the growth of the cluster sizes is not uniform. Such irregular growth of the clusters can be attributed to sensitive dependence on other parameters of the system such as initial conditions. On complete synchronization, the locking frequency for the array is computed to be 1.207. This frequency is less than the average of the limit cycle frequencies of the individual LCOs in the array, which is 1.230. Because the array locks at a lower frequency, the stiffest oscillator, with the highest detuning parameter, requires the highest value of coupling to join the self-synchronized array. An averaging method to estimate the locking frequency of the array is given in Sec. 4.3.

Fig. 4 shows an intermediate cluster state for a single coupling strength $V^2 = 0.0012$, and average detuning value $\bar{\kappa} = 1.168$. For these parameters four clusters of different sizes are formed. The FFT plots corresponding to the limit cycle oscillations of each of the eight LCOs in the array are plotted and the amplitude peaks are shown in the zoomed inset. The coincidence of the peaks implies synchronization of the oscillators. Side bands are present in the FFT plots due to the coupling interactions between the oscillators. The first oscillator is vibrating at its uncoupled limit cycle frequency of 1.173. The second, third, and fourth oscillators with uncoupled limit cycle frequencies of $1.19, 1.206$ and 1.221, form a cluster of size three and lock at an intermediate frequency of 1.204. The fifth and the sixth oscillators with uncoupled limit cycle frequencies of 1.238 and 1.254, form a cluster of size two and lock at a frequency of 1.245. The seventh and the eighth oscillators with uncoupled limit cycle frequencies of

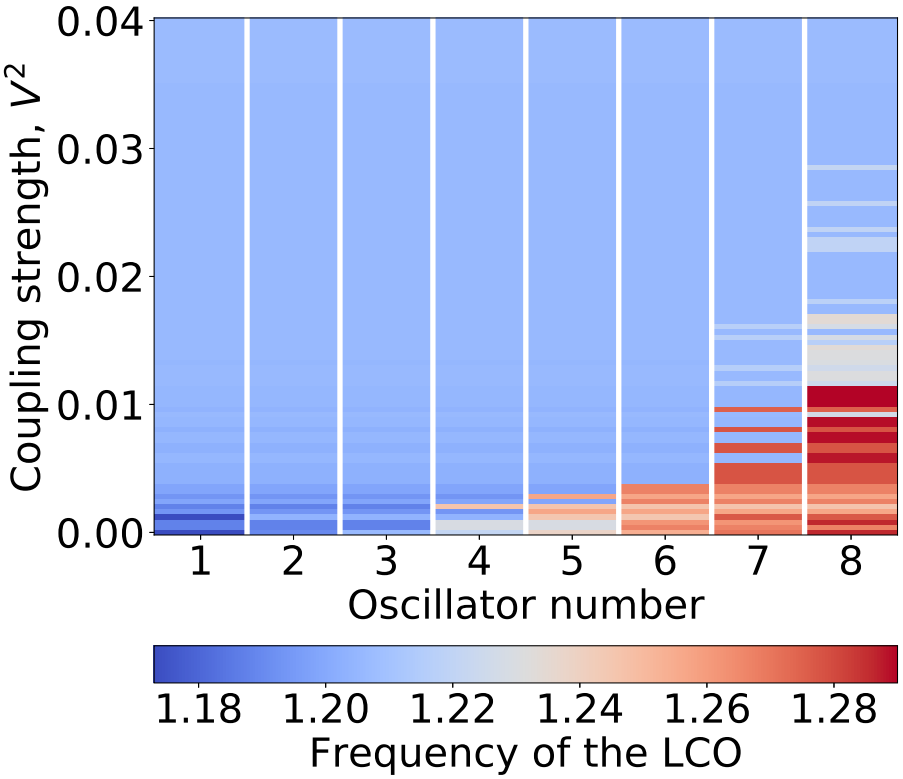

Figure 3: The frequencies of coupled LCOs in an array with detuning $\bar{\kappa} = 1.168$ as the coupling strength is increased show the route to self-synchronization. The uncoupled frequencies are $(1.173, 1.19, 1.206, 1.221, 1.238, 1.254, 1.27, 1.286)$. Frequency-locked clusters begin to form at weak coupling strengths. At high coupling, the array self-synchronizes at a frequency of 1.207. The calculations are started with zero initial conditions.

1.27 and 1.286, form a cluster of size two and lock at a frequency of 1.277. It can be noted that the locking frequency of each cluster is less than the average of the uncoupled limit cycle frequencies of the LCOs constituting the cluster. The existence of frequency-locked cluster states differentiates the dynamics of large LCO arrays from that of two coupled LCOs.

4.2. Sensitivity to initial conditions

We noted from Fig. 2 that the boundaries of the Arnold tongues are indistinct and from Fig. 3 that the progression to complete self-synchronization is nonuniform. It has been shown in other work that there could be multiple co-

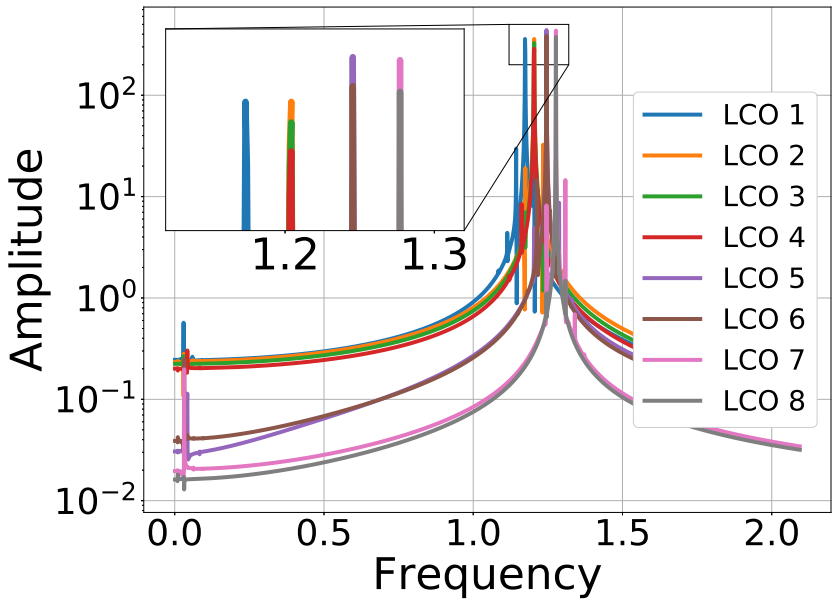

Figure 4: Frequency spectrum for an array of eight coupled LCOs with average detuning $\bar{\kappa} = 1.168$ and coupling strength $V^2 = 0.0012$. Frequency-locked clusters are formed as can be seen from the coincidence of the amplitude peaks in the inset. The locked LCO frequencies are $(1.173, 1.204, 1.245, 1.277)$. The uncoupled LCO frequencies at this detuning are $(1.173, 1.19, 1.206, 1.221, 1.238, 1.254, 1.27, 1.286)$.

existing stable states for a dynamical system [33] and that the initial conditions could dictate the final state of the system [34]. The initial condition space is explored for the array of MEMS LCOs using a probability map in the average detuning vs. coupling strength space. Again, 101 equally spaced values of the average detuning parameter, $\bar{\kappa} \in [0.65, 1.35]$ and 101 equally spaced values of the coupling strength, $V^2 \in [0, 0.04]$ are used. The calculations are performed for each $(\bar{\kappa},\ V^2)$ pair starting with 25 random initial displacements chosen in the interval $[0, 0.4)$. The probability of reaching complete self-synchronization from this set of initial conditions is shown in Fig. 5. There is a tongue-like region corresponding to certain complete self-synchronization, which is centered at $\bar{\kappa} = 1$ and has the same qualitative shape as the innermost Arnold tongue in Fig. 2. It can be noted that the ranges of the parameters in both the fig-

ures are the same. The region of uncertainty, lying on the boundary of the tongue, explains the indistinct boundaries of the innermost Arnold tongue and reveals that the system has sensitive dependence on initial conditions. Such a plot also provides the appropriate choice of parameters for achieving robust self-synchronization, which may be desired for sensing applications. This map, however, does not address the probability of the formation of smaller clusters, but it can be deduced that there would be a thin region of uncertainty for the formation of clusters of different sizes corresponding to each of the eight Arnold tongues in Fig. 2.

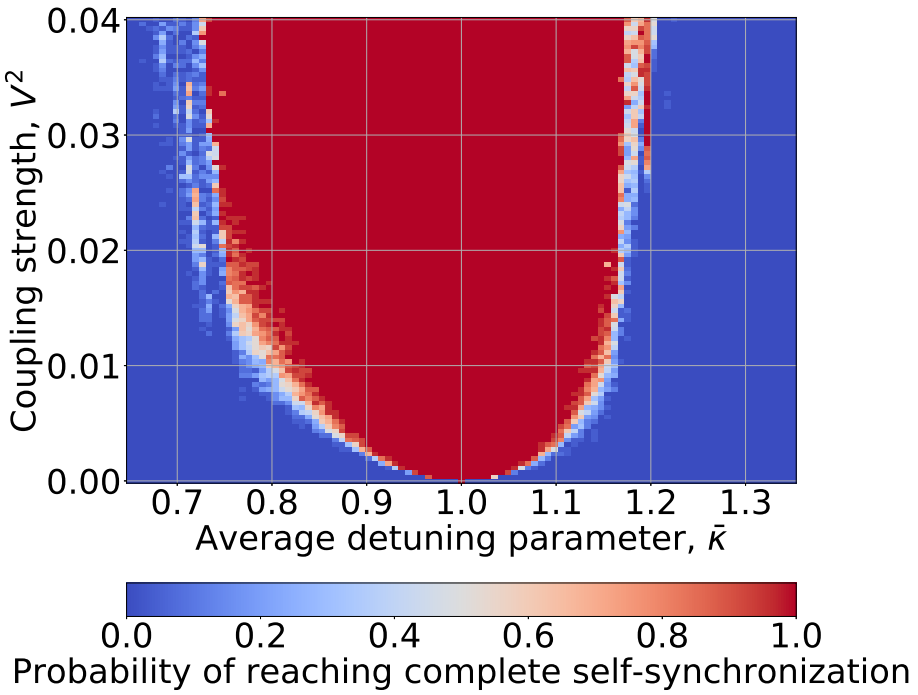

Figure 5: Probability map showing the fraction of initial conditions in the detuning vs. coupling strength parameter space that lead to complete self-synchronization. Twenty five initial displacements are randomly chosen in an interval $[0, 0.4)$ for each detuning and coupling combination. There is sensitive dependence on initial conditions at the border of the tongue.

4.3. Estimation of the locking frequency

In the discussion of Fig.3, it was observed that for high coupling strengths, all the LCOs in the array oscillate at a single locking frequency which is less than the average of the limit cycle frequencies of the uncoupled LCOs. A method to estimate this locking frequency is considered. Time traces of self-synchronized arrays reveal that for high coupling strengths, not only do the frequencies match, but so do the phase and amplitude of oscillation. The higher the coupling the more identical the oscillators behave. In the strong coupling limit, it can be assumed that all the dynamical variables, $z_i(t)$ and $T_i(t)$, coincide at $z(t)$ and $T(t)$, respectively. Eqs. 1-4 can be averaged over the entire array. The technique of averaging over a self-synchronized network of oscillators has been applied in earlier works to phase-only oscillators to obtain the conditions for synchronization [35]. Upon averaging the governing equations over the array, the coupling terms cancel out and the different detuning parameters, κ_1-κ_8, are replaced with one average detuning parameter $\bar{\kappa}$. We get,

$$\ddot{z} + \frac{\dot{z}}{Q} + \bar{\kappa}(1 + CT)z + \beta z^3 = DT, \tag{5}$$

$$\dot{T} = -BT + HP_{\text{laser}}[\alpha + \gamma \sin^2(2\pi(z - \bar{z}))]. \tag{6}$$

Since we are considering the case of self-synchronization, the inertial drive is absent and $E = 0$. We get a single LCO, which will be termed as the *equivalent oscillator*, in place of the entire self-synchronized array. The limit cycle frequency of the equivalent oscillator, which is independent of the coupling strength, is compared to the locking frequency of the LCO array, at weak coupling, $V^2 = 0.01$, and at strong coupling, $V^2 = 100$, and is shown in Fig. 6. All the calculations are done using numerical integration. For an array with no detuning, corresponding to $\bar{\kappa} = 1$, the frequencies trivially match. For a detuned array, the equivalent oscillator describes the array better in the strong coupling regime than in the weak coupling regime.

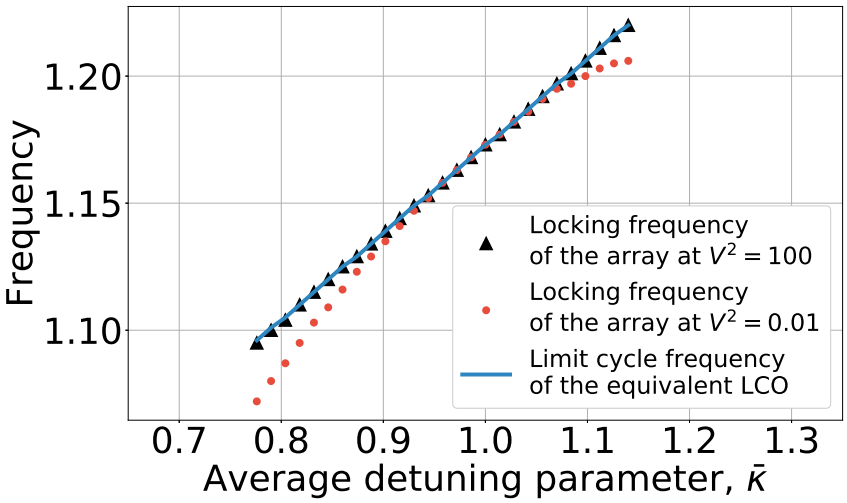

Figure 6: Comparison of the limit cycle frequency of the equivalent oscillator and the locking frequency of the array of eight oscillators for weak coupling $V^2 = 0.01$ and strong coupling $V^2 = 100$, as the detuning in the system is varied. The frequency of the equivalent oscillator is a better estimate for the locking frequency of the array for higher coupling strengths.

Thus, a self-synchronized array of LCOs can be replaced by a single equivalent oscillator, characterized by the average detuning parameter of the array, $\bar{\kappa}$. In Sec. 5.2, when the array is subjected to external inertial forcing, the array would be substituted by the equivalent oscillator, because entrainment of the self-synchronized array to the drive is of importance. The reduction of a list of equations to that of a single oscillator makes the application of the perturbation theory more tractable.

5. Entrainment of an array of coupled LCOs by an inertial drive

5.1. Dependence on coupling strength, inertial drive strength and inertial drive frequency

In this section, a numerical analysis is done to describe the entrainment characteristics of an array of LCOs driven externally by an inertial forcing function. The array itself can be detuned and additionally, there might be a mismatch

between the frequency of the inertial drive and the limit cycle frequencies of the individual LCOs. It should be noted that all the oscillators experience the same inertial drive. If the LCOs vibrate at the same frequency as the inertial drive then they are said to be entrained and the entrainment characteristics of the array are studied for a range of coupling strengths, inertial drive strengths, and inertial drive frequencies. The calculations are performed using the numerical procedure described in Sec. 3.

In Fig. 7, the average detuning parameter for the array is fixed at $\bar{\kappa} = 1.07$ and the inertial drive frequency is fixed at $\omega_d = 1.4$. A parametric sweep is performed with 101 equally spaced values of the inertial drive strength, $E \in [0, 0.04]$, and 101 equally spaced values of the coupling strength, $V^2 \in [0, 0.04]$. The calculations are started with zero initial conditions. For low coupling strengths, the transition from drift to full entrainment involves the formation of entrained clusters. As the inertial drive strength is increased the number of LCOs in the entrained cluster increases and beyond a threshold value of the drive strength the array is fully entrained. As the coupling strength is increased, the drive strength required to entrain the array saturates at a constant value. This is seen as the vertical shoulder in Fig. 7. Also, in the strong coupling regime, the transition from a state of drift to full entrainment bypasses the formation of clusters.

In Fig. 8, we switch to looking at another slice of the parameter space and fix the average detuning parameter for the array at $\bar{\kappa} = 1.07$ and the coupling strength at a low value, $V^2 = 0.0016$. A parametric sweep is performed with 101 equally spaced values of the inertial drive frequency, $\omega_d \in [0.9, 1.5]$, and 101 equally spaced values of the inertial drive strength, $E \in [0, 0.04]$. The calculations are started with zero initial conditions. There is an Arnold tongue corresponding to full entrainment of the array with regions of partial entrainment on the border. Since the locking frequency corresponding to self-synchronization of the array is 1.195, for drive frequencies close to this value, the drive strength required to entrain the system is low. The more the drive frequency deviates from this value the higher the drive strength required to fully entrain the ar-

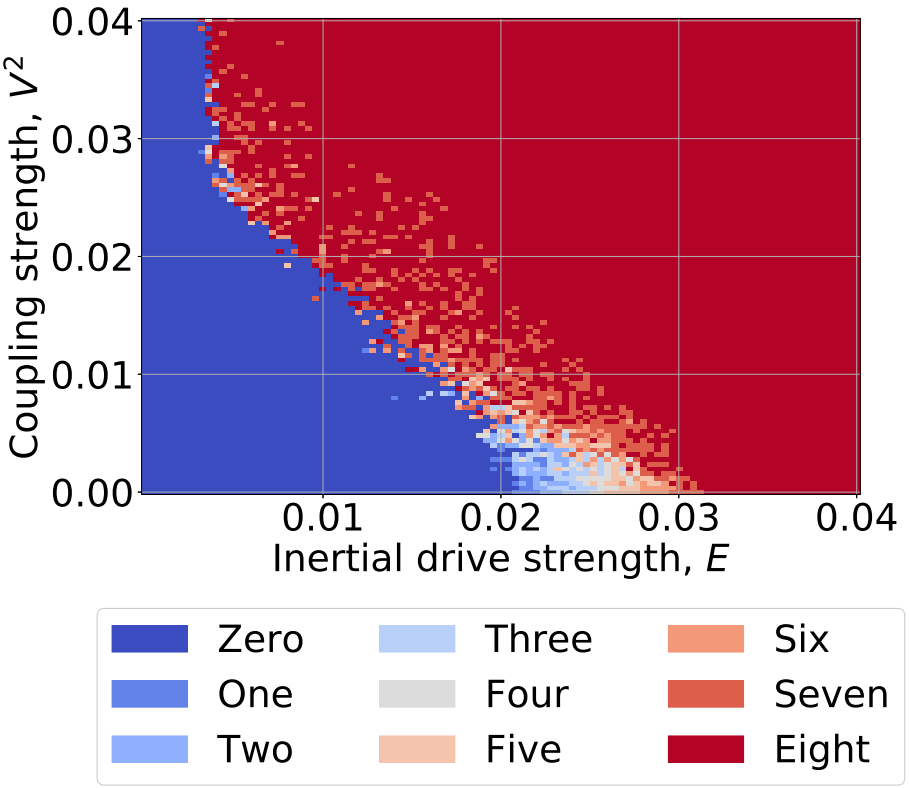

Figure 7: The number of oscillators, in an array of eight coupled LCOs, entrained by an inertial drive, plotted in the inertial drive strength vs. coupling strength parameter space. The inertial drive frequency is fixed at $\omega_d = 1.4$. The average detuning parameter of the array is fixed at $\bar{\kappa} = 1.07$ with uncoupled and undriven LCO frequencies of $(1.173, 1.18, 1.187, 1.194, 1.2, 1.207, 1.214, 1.22)$ and an undriven locking frequency of 1.195. The calculations are started with zero initial conditions. There are entrained clusters at weak coupling but not at strong coupling.

ray. In the weak coupling regime smaller entrained clusters can be observed but for higher coupling strengths the transition from a state of complete drift to complete entrainment would be immediate.

315 The features of the system at high coupling strengths are reminiscent of the features of a single LCO [12] and motivates us to analyze the entrainment characteristics of the array using the concept of the equivalent oscillator, described in Sec. 4.3. Perturbation theory is used to estimate the threshold drive strength for full entrainment of a strongly coupled array in Sec. 5.2.

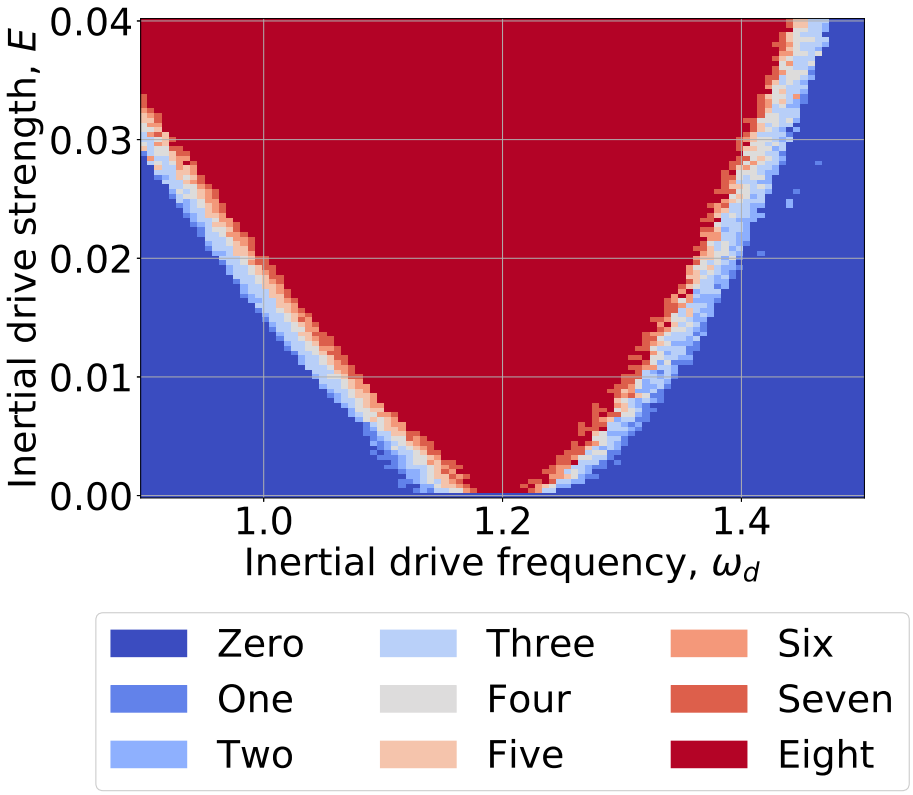

Figure 8: The number of oscillators, in an array of eight coupled LCOs, entrained by an inertial drive, plotted in the inertial drive frequency vs. inertial drive strength parameter space. The coupling strength in the array is fixed at a low value of $V^2 = 0.0016$. The average detuning parameter of the array is fixed at $\bar{\kappa} = 1.07$ with uncoupled, undriven LCO frequencies of $(1.173, 1.18, 1.187, 1.194, 1.2, 1.207, 1.214, 1.22)$ and an undriven locking frequency of 1.195. The calculations are started with zero initial conditions. In this weak coupling regime, an Arnold tongue is seen corresponding to full entrainment flanked by thin regions of partial entrainment.

5.2. Perturbation analysis of threshold drive strength for entrainment

In this section, we compute the minimum drive strength to fully entrain a completely self-synchronized array of LCOs. The array is characterized by a single equivalent oscillator as described in Sec. 4.3. The method of two-variable expansion, a perturbation method, is applied to the equivalent oscillator after appropriate scaling and the stability of the fixed points of the system is analyzed to look for entrained oscillations. This analysis also reveals a sequence of bifurcations that occurs as the drive strength is increased. The perturbation

scheme applies only to weakly nonlinear oscillators and hence a scaling term, denoted by ϵ, is introduced in Eqs. 5-6. Furthermore, for small values of ϵ, the sine-squared term in Eq. 6 is approximated by the first two terms in its Taylor-series expansion, resulting in the following set of governing equations,

$$\ddot{z} + \epsilon\frac{\dot{z}}{Q} + \bar{\kappa}(1+\epsilon CT)z + \epsilon\beta z^3 = \epsilon DT + \ldots \\ \ldots + \epsilon E\sin(\omega_d t), \tag{7}$$

$$\dot{T} = -BT + HP_{\text{laser}}\left[\epsilon\alpha + \gamma\left(4\pi^2(z-\epsilon\bar{z})^2 - \ldots \right.\right. \\ \left.\left. \ldots - (16\pi^4/3)(z-\epsilon\bar{z})^4\right)\right]. \tag{8}$$

Two timescales are introduced in the solution, with $\xi = \omega_d t$ representing stretched time, and $\eta = \epsilon t$ representing slow time. This allows us to write, $\dot{z} = \omega_d z_\xi + \epsilon z_\eta$, $\ddot{z} = \omega_d^2 z_{\xi\xi} + 2\omega_d\epsilon z_{\xi\eta} + \epsilon^2 z_{\eta\eta}$ and $\dot{T} = \omega_d T_\xi + \epsilon T_\eta$. Here, the subscripts, ξ and η, represent partial differentiation with respect to the corresponding variable. The dynamical quantities z and T are expanded in power series to get,

$$z(\xi,\eta) = z_0(\xi,\eta) + \epsilon z_1(\xi,\eta) + ..., \tag{9}$$

$$T(\xi,\eta) = T_0(\xi,\eta) + \epsilon T_1(\xi,\eta) + ... \tag{10}$$

We let the inertial drive frequency be nearly equal to the natural frequency of the linearized and unperturbed oscillator and write,

$$\omega_d = \sqrt{\bar{\kappa}} + \epsilon\omega_1 + ... \tag{11}$$

Here, ω_1 represents the frequency detuning between the oscillator and the inertial drive. Substituting Eqs. (9), (10) and (11) into Eqs. (7)-(8) results in

the following forms of the solution at the zeroth order,

$$z_0(\xi,\eta) = a(\eta)\cos\xi + b(\eta)\sin\xi, \tag{12}$$

$$\begin{aligned} T_0(\xi,\eta) &= c_0(\eta) + c_1(\eta)\cos\xi + c_2(\eta)\sin\xi + ... \\ &... + c_3(\eta)\cos 2\xi + c_4(\eta)\sin 2\xi + c_5(\eta)\cos 3\xi + ... \\ &... + c_6(\eta)\sin 3\xi + c_7(\eta)\cos 4\xi + c_8(\eta)\sin 4\xi, \end{aligned} \tag{13}$$

where $c_i(\eta)$ can be solved for in terms of $a(\eta)$ and $b(\eta)$. Substituting Eqs. (12)-(13) and removing the resonant terms from Eq. (7) at the first order, results in two first-order differential equations in $a(\eta)$ and $b(\eta)$. The computer algebra is performed using Maxima 5.42.2 [36] and the code to perform the calculation is given in the Supplemental material [37]. The values of the fixed parameters are substituted from Tab. 1. The detuning parameter is set at $\bar{\kappa} = 1$. The laser power is set at a high value of $P_{\text{laser}} = 0.02$ W in order to obtain limit cycle oscillations. Transforming to polar coordinates, $a(\eta) = \rho(\eta)\cos(\theta(\eta))$ and $b(\eta) = \rho(\eta)\sin(\theta(\eta))$, the equations that describe the variation of the amplitude in slow time are obtained,

$$\begin{aligned} \frac{d\rho}{d\eta} &= -\frac{E\cos\theta}{2} - 0.9656\rho^5 + 0.07338\rho^3 - ... \\ &... - 4.032\times 10^{-4}\rho, \end{aligned} \tag{14}$$

$$\frac{d\theta}{d\eta} = \omega_1 + \frac{E\sin\theta}{2\rho} + 26\rho^4 - 8.445\rho^2. \tag{15}$$

Eqs. 14-15 are referred to as the *slow flow equations*. Fixed points, (ρ^*, θ^*), in the slow flow equations correspond to entrained oscillations of the single equivalent oscillator described by Eqs. (7)-(8), whereas periodic solutions of the slow flow equations correspond to quasi-periodic oscillations of the equivalent oscillator. Let the Jacobian matrix corresponding to Eqs. (14)-(15) be M. A fixed point would be stable if, for the Jacobian matrix evaluated at the point, the trace is negative, $tr(M) < 0$, and the determinant is positive, $det(M) > 0$ [38]. Eliminating θ^* and solving for ρ^*, results in the following relation between

the inertial drive strength, E, and the fixed point coordinate ρ^*,

$$
\begin{aligned}
E^2 &= 208\rho^{*6}\omega_1 - 67.56\rho^{*4}\omega_1 + 4\rho^{*2}\omega_1^2 + \dots \\
&\dots + 2.708 \times 10^3\rho^{*10} - 1.757 \times 10^3\rho^{*8} + 285.3\rho^{*6} - \dots \\
&\dots - 2.367 \times 10^{-4}\rho^{*4} + 6.503 \times 10^{-7}\rho^{*2}
\end{aligned} \tag{16}
$$

In Fig. 9, Eq.(16) is plotted for a fixed detuning $\omega_1 = 1$, and the linear stability of the fixed points, obtained from the Jacobian matrix, M, is shown. There are five qualitatively different phase portraits in the $\rho - \theta$ phase plane for different ranges of the drive strength. These regions are marked (a)-(e) in the figure. The phase planes were numerically plotted and examined on pplane [39] and their sketches are shown in Fig. 10. This figure also reveals the sequence of bifurcations that the oscillator undergoes as the drive strength is increased.

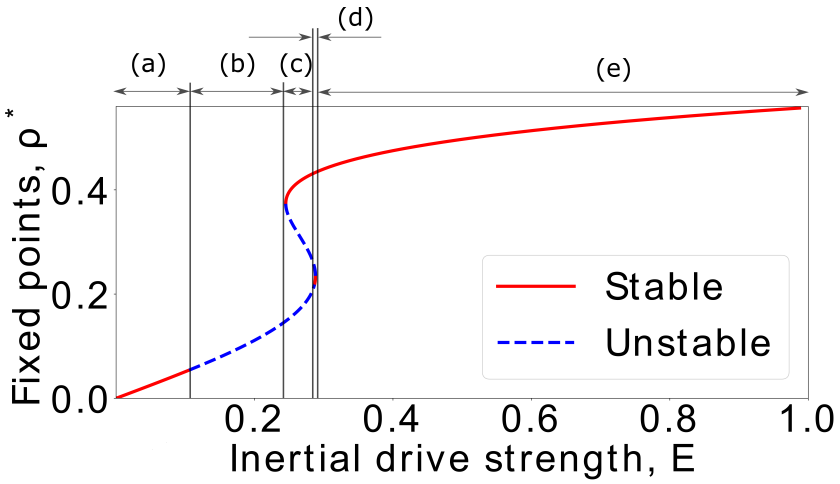

Figure 9: Fixed points of the slow flow system of Eqs. 14-15 and their stability calculated using linearization. The curve itself is given by Eq.16 and the frequency detuning of the drive is fixed using $\omega_1 = 1$. The labels (a)-(e) correspond to Figs. 10a-10e.

Numerical integration of the slow flow equations reveals that, in region (a), $E \in (0, 0.1053)$, there is a stable spiral surrounded by an unstable limit cycle and a larger stable limit cycle as shown in Fig. 10a. Since the basin of attraction

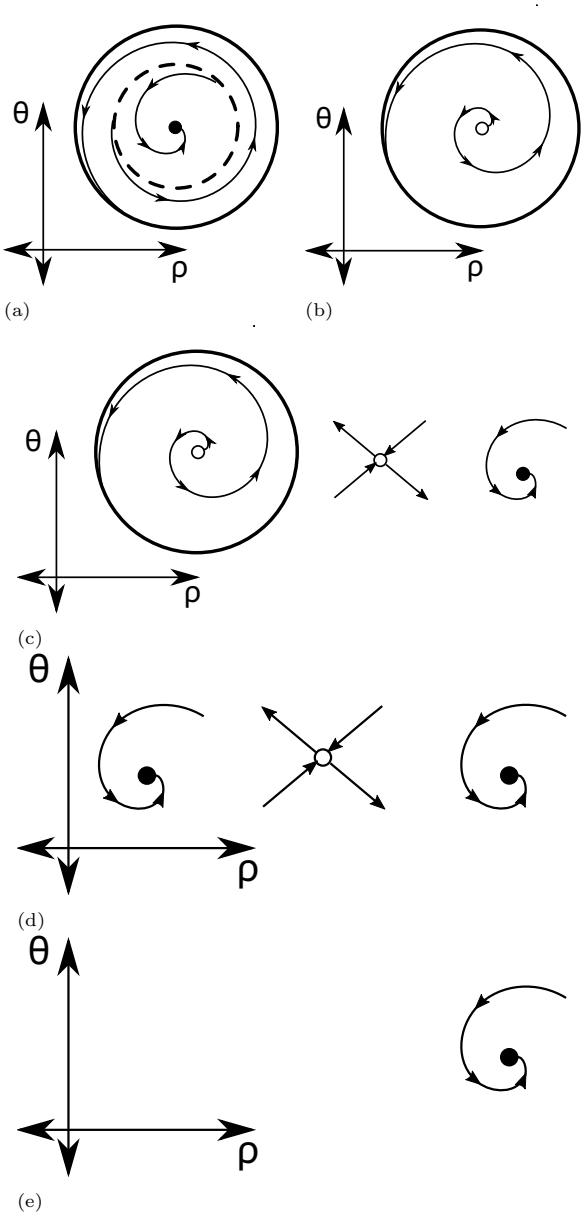

Figure 10: Sketches of the equilibrium points corresponding to the slow flow system of Eqs. 14-15 with $\omega_1 = 1$, and the associated phase portraits. The bifurcation sequence is shown as the inertial drive strength, E, is increased. (a) A stable spiral surrounded by an unstable limit cycle and a stable limit cycle for $E \in (0, 0.1053)$. (b) An unstable spiral, resulting from a subcritical Hopf bifurcation, surrounded by a stable limit cycle, for $E \in (0.1054, 0.2451)$. (c) Two fixed points, a saddle point and a stable node, born in a saddle-node bifurcation. For $E \in (0.2452, 0.2867)$, the stable node converts to a stable spiral. (d) A stable spiral, resulting from a supercritical Hopf bifurcation, for $E \in (0.2868, 0.2880)$. (e) A globally stable spiral with the other two fixed points vanishing in a saddle-node bifurcation, for $E > 0.2881$.

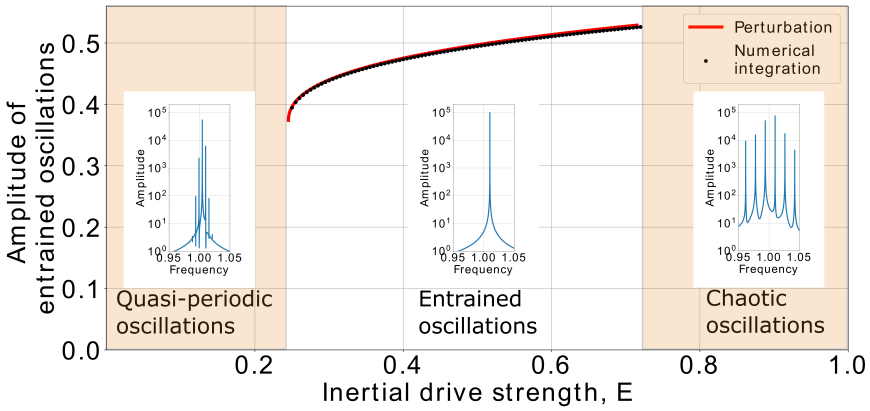

Figure 11: Three qualitatively different behavior of the driven oscillator corresponding to Eqs. 14-15 for $\omega_1 = 1$. For low drive strengths the system shows quasi-periodic oscillations whereas for high drive strengths the system shows chaotic oscillations. For an intermediate range of drive strengths, the system is entrained and the amplitude of oscillation predicted by the perturbation theory is verified using direct numerical integration. The frequency spectrum for each of the three regimes is shown in the insets.

for the spiral is relatively small, most initial conditions end up on the stable limit cycle. At $E \approx 0.1053$, the unstable limit cycle engulfs the spiral, rendering it unstable, in a subcritical Hopf bifurcation. In region (b), $E \in (0.1054, 0.2451)$, the stable limit cycle is the only attractor in the phase plane as shown in Fig. 10b. Thus, for small drive strengths, $E \in (0, 0.2451)$, the perturbation theory predicts that the oscillator would exhibit quasi-periodic motion. At $E \approx 0.2451$, a saddle point and a stable node are born outside the stable limit cycle, in a saddle-node bifurcation of fixed points. With an increase in the drive strength the stable node converts into a stable spiral and the fixed points are shown in Fig. 10c. In region (c), $E \in (0.2452, 0.2867)$, the stable limit cycle shrinks around the unstable spiral causing the stable spiral to have a larger basin of attraction. At $E \approx 0.2867$, the stable limit cycle engulfs the unstable spiral in a supercritical Hopf bifurcation, resulting in a stable spiral as shown in Fig. 10d. In region (d), $E \in (0.2868, 0.2880)$, the stable spiral born in the saddle-node bifurcation has a larger basin of attraction resulting in entrained solutions of the original system for high drive strengths. At $E \approx 0.2880$, the saddle point and the new stable

spiral collide and vanish in a saddle-node bifurcation of fixed points, resulting in the original spiral being globally stable as shown in Fig. 10e. Thus, for higher drive amplitudes, in region (e), $E > 0.2452$, the perturbation theory predicts that the oscillator would be entrained by the inertial drive.

The entrainment characteristics predicted by the perturbation theory are compared to the results from the numerical resolution of Eqs. 7-8 with the same parameters as the perturbation theory, with $\bar{\kappa} = 1$, $\omega_1 = 1$ and a small value of the scaling parameter, $\epsilon = 0.01$. This results in an inertial drive frequency of $\omega_d = \sqrt{\bar{\kappa}} + \epsilon\omega_1 = 1 + 0.01 \times 1 = 1.01$, from Eq. 11. In the numerical calculations, the system is started with initial conditions $(z(0), \dot{z}(0), T(0)) = (0.2, 0, 0)$. The computation predicts three qualitatively different behaviors as the drive strength, E, is increased. These are shown in Fig. 11. For low drive strengths up to $E \approx 0.245$, the FFT spectrum corresponding to the LCO motion shows two prominent peaks which are characteristic of quasi-periodic oscillations. A sample FFT spectrum is shown in the inset for $E = 0.02$. For $E \in (0.245, 0.74)$, the numerical calculations show entrained solutions with a single peak in the FFT spectrum corresponding to the inertial drive frequency. A sample FFT spectrum is shown in the inset for $E = 0.4$. The amplitude of oscillation due to the perturbation theory and given by Eq. 16 is plotted for this range of drive strengths and compared with the amplitudes of oscillation from numerical integration. The plot shows that the amplitudes calculated using the two methods agree. In particular, the minimum drive strength, or the *threshold drive strength for entrainment*, is well-approximated by the perturbation theory. A third qualitatively different behavior is obtained from the numerical solution for $E > 0.74$. A sample FFT spectrum is shown in the inset for $E = 0.9$. The FFT shows a broad spectrum of frequencies, and for a system of low order (one to three), this suggests the presence of chaotic oscillations [40]. Chaos at large drive strength has not been investigated further since the focus of this work is on the synchronization of the system. Nevertheless, transitions from entrained solutions to chaotic solutions at large drive strengths have been noted previously in mechanically coupled MEMS resonators [41]. The perturbation analysis in

this work is unable to capture this transition since the method is applicable at low drive strengths.

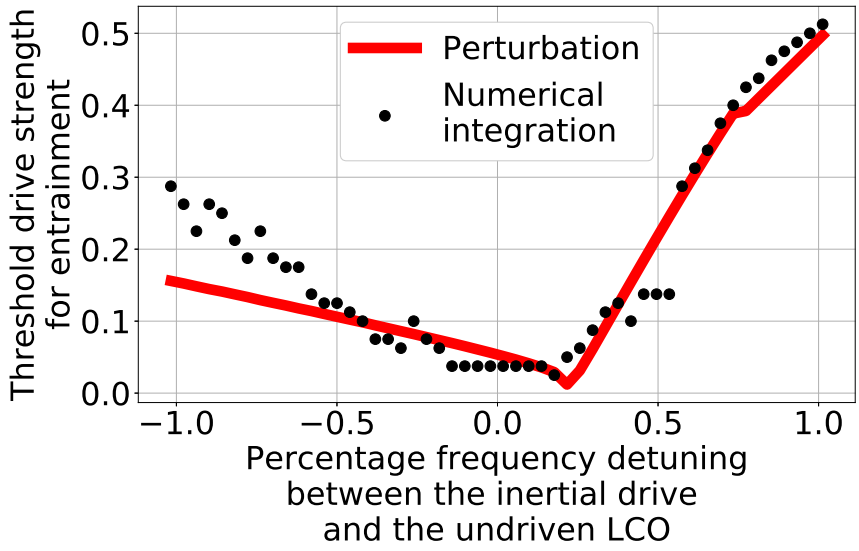

Figure 12: Comparison of the threshold drive strength for entrainment calculated using Eq. 16 from perturbation analysis and using direct numerical integration of Eqs. 7-8 with arbitrary initial conditions $(z(0), \dot{z}(0), T(0))$ in the interval $[0, 0.2)$. The tongue-like shape is analogous to Fig. 8.

Perturbation theory was used to predict the threshold drive strength for entrainment for a single value of detuning $\omega_1 = 1$ as shown in Fig. 11. A similar perturbation analysis is done for a range of different detuning values. The threshold strength for entrainment is obtained by selecting the drive strength corresponding to the saddle-node bifurcation of fixed points resulting in the birth of the stable spiral. This threshold is also obtained by direct numerical integration of Eqs. (7)-(8). This is done by performing the calculations for a range of drive strengths and selecting the minimum value for which frequency entrainment is seen. In the numerical calculation, the initial conditions, $(z(0), \dot{z}(0), T(0))$, are chosen randomly from the interval, $[0, 0.2)$. Further, the undriven limit cycle frequency of the LCO is numerically calculated to $\omega_{\mathrm{LCO}} = 1.0046$. Using this value, the percentage frequency detuning between

the inertial drive and the undriven LCO is defined as $100 \times (\omega_d - \omega_{\mathrm{LCO}})/\omega_{\mathrm{LCO}}$. In Fig. 12, the threshold drive strength for a range of percentage detuning from -1% to $+1\%$, calculated using perturbation theory is compared to the values obtained by numerical integration. Both methods predict the existence of tongue-like region centered at zero detuning and agree on the numerical values. These curves qualitatively capture the trend shown in Fig. 8. The results relate to the choice of inertial drive strengths for achieving entrainment in experiments.

6. Summary and conclusions

In this work, the dynamics of a coupled array of eight MEMS oscillators was analyzed and the emergence of synchronization was considered for the undriven network as well as the inertially driven system. Numerical calculations reveal that some of the dynamical behavior of the array is similar to that of two coupled oscillators: presence of Arnold tongues in parameter spaces, sensitive dependence to initial conditions. The important distinction between two coupled LCOs and a larger array of coupled LCOs is the existence of frequency-locked cluster states. Averaging over the array is used to estimate the frequency of a completely self-synchronized array and this lets us replace the array with a single equivalent oscillator for further analytical calculations. For the inertially driven array, in the strongly coupled regime, a threshold drive strength is identified and it is independent of the coupling strength. The equivalent oscillator is used to qualitatively capture the entrainment trends of the self-synchronized array. This analysis reveals a bifurcation sequence that the oscillator goes through before getting entrained by the inertial drive. Numerical calculations also reveal that the system possibly transitions to a state of chaos for very high drive strengths.

The characteristics of the system are summarized as follows.The laser power must be above a threshold value for limit cycles to exist in the system [11]. As the detuning in the system is increased, the coupling strength required for complete self-synchronization increases. The transition to fully self-synchronized

state occurs when the coupling strength is approximately equal to the difference in the linear stiffness between neighboring oscillators. The system reaches complete synchronization via the formation of clusters and the cluster formation is non-uniform as the coupling strength is increased. At the boundaries of Arnold tongues, full synchronization of the system depends sensitively on initial conditions. For an externally driven system, as the coupling strength is increased, the inertial drive strength required to entrain the system decreases. Additionally, as the mismatch in the frequency between the inertial drive and the system is increased, the inertial drive strength required to entrain the system increases.

The primary motivation of this analysis was to uncover the qualitative nature of the dynamics of the proposed MEMS LCO array so that we know what to look for in experiments and to provide guidance in the design of the MEMS array and experimental parameters. Future work could also address questions pertaining to the response in the presence of noise terms, the locking of frequencies at other integer ratios such as $1:2$, $1:3$, $2:3$ etc.

7. Acknowledgments

This material is based upon work supported by the National Science Foundation (NSF) under grant number CMMI-1634664. This work used allocation TG-MSS170032 at the Extreme Science and Engineering Discovery Environment (XSEDE), which is supported by NSF grant number ACI-1548562. Specifically, it used the Bridges system, which is supported by NSF award number ACI-1445606, at the Pittsburgh Supercomputing Center (PSC).

References

[1] X. Feng, C. White, A. Hajimiri, and M. L. Roukes, Nature Nanotechnology **3**, 342 (2008).

[2] A. W. Barnard, M. Zhang, G. S. Wiederhecker, M. Lipson, and P. L. McEuen, Nature **566**, 89 (2019).

[3] M. Zhang, G. Luiz, S. Shah, G. Wiederhecker, and M. Lipson, Applied Physics Letters **105**, 051904 (2014).

[4] Y. Lu and D. A. Horsley, Journal of Microelectromechanical Systems **24**, 1142 (2015).

[5] M. A. Rasouli and B. Bahreyni, Applied Physics Letters **98**, 243508 (2011).

[6] I. Bargatin, E. Myers, J. Aldridge, C. Marcoux, P. Brianceau, L. Duraffourg, E. Colinet, S. Hentz, P. Andreucci, and M. Roukes, Nano Letters **12**, 1269 (2012).

[7] S. Marquez, M. Alvarez, J. A. Plaza, L. Villanueva, C. Dominguez, and L. M. Lechuga, Applied Physics Letters **111**, 113101 (2017).

[8] D. Rugar, R. Budakian, H. Mamin, and B. Chui, Nature **430**, 329 (2004).

[9] J. Van Beek and R. Puers, Journal of Micromechanics and Microengineering **22**, 013001 (2011).

[10] A. Jenkins, Physics Reports **525**, 167 (2013).

[11] K. Aubin, M. Zalalutdinov, T. Alan, R. B. Reichenbach, R. Rand, A. Zehnder, J. Parpia, and H. Craighead, Journal of Microelectromechanical Systems **13**, 1018 (2004).

[12] M. Pandey, R. Rand, and A. Zehnder, Communications in Nonlinear Science and Numerical Simulation **12**, 1291 (2007).

[13] N. Diamant, P. Rose, and E. Davison, American Journal of Physiology-Legacy Content **219**, 1684 (1970).

[14] S. H. Strogatz, Journal of Mathematical Biology **25**, 327 (1987).

[15] G. Bloch, E. D. Herzog, J. D. Levine, and W. J. Schwartz, Proceedings of the Royal Society B: Biological Sciences **280**, 20130035 (2013).

[16] M. H. Matheny, J. Emenheiser, W. Fon, A. Chapman, A. Salova, M. Rohden, J. Li, M. H. de Badyn, M. Pósfai, L. Duenas-Osorio, *et al.*, Science **363**, eaav7932 (2019).

[17] S.-B. Shim, M. Imboden, and P. Mohanty, Science **316**, 95 (2007).

[18] C. B. Wallin, R. De Alba, D. Westly, G. Holland, S. Grutzik, R. H. Rand, A. T. Zehnder, V. A. Aksyuk, S. Krylov, and B. R. Ilic, Physical Review Letters **121**, 264301 (2018).

[19] M. Zhang, G. S. Wiederhecker, S. Manipatruni, A. Barnard, P. McEuen, and M. Lipson, Physical Review Letters **109**, 233906 (2012).

[20] S. T. Habermehl, N. Bajaj, S. Y. Shah, D. D. Quinn, D. Weinstein, and J. F. Rhoads, Nonlinear Dynamics , 1 (2019).

[21] M. Zhang, S. Shah, J. Cardenas, and M. Lipson, Physical Review Letters **115**, 163902 (2015).

[22] D. K. Agrawal, J. Woodhouse, and A. A. Seshia, Physical Review Letters **111**, 084101 (2013).

[23] S. Krylov, S. Lulinsky, B. R. Ilic, and I. Schneider, Applied Physics Letters **105**, 071909 (2014).

[24] Y. Linzon, B. Ilic, S. Lulinsky, and S. Krylov, Journal of Applied Physics **113**, 163508 (2013).

[25] M. Napoli, W. Zhang, K. Turner, and B. Bamieh, Journal of Microelectromechanical Systems **14**, 295 (2005).

[26] D. B. Blocher, A. T. Zehnder, and R. H. Rand, Journal of Microelectromechanical Systems **22**, 835 (2013).

[27] A. T. Zehnder, R. H. Rand, and S. Krylov, International Journal of Non-Linear Mechanics **102**, 92 (2018).

[28] S. Krylov, N. Molinazzi, T. Shmilovich, U. Pomerantz, and S. Lulinsky, in *ASME 2010 International Design Engineering Technical Conferences and Computers and Information in Engineering Conference* (American Society of Mechanical Engineers Digital Collection, 2010) pp. 601–611.

[29] D. Blocher, *Optically driven limit cycle oscillations in MEMS*, Ph.D. thesis, Cornell University (2012).

[30] T. Chakraborty and R. H. Rand, International Journal of Non-Linear Mechanics **23**, 369 (1988).

[31] A. Pikovsky, J. Kurths, M. Rosenblum, and J. Kurths, *Synchronization: A Universal Concept in Nonlinear Sciences*, Vol. 12 (Cambridge university press, 2003).

[32] T. E. Lee, C.-K. Chan, and S. Wang, Physical Review E **89**, 022913 (2014).

[33] R. H. Rand, A. T. Zehnder, B. Shayak, and A. Bhaskar, Nonlinear Dynamics **99**, 73 (2020).

[34] M. H. Matheny, M. Grau, L. G. Villanueva, R. B. Karabalin, M. C. Cross, and M. L. Roukes, Physical Review Letters **112**, 014101 (2014).

[35] F. Mori, Physical Review Letters **104**, 108701 (2010).

[36] Maxima, Maxima, A Computer Algebra System. Version 5.34.1 (2014).

[37] See supplemental material at [url will be inserted by publisher] for the maxima code to perform the computer algebra to remove the resonant terms and obtain the slow flow equations.

[38] R. H. Rand, Lecture notes on nonlinear vibrations (2012).

[39] J. C. John C. Polking, pplane, `https://math.rice.edu/~dfield/dfpp.html`.

[40] F. C. Moon, *Chaotic and Fractal Dynamics: Introduction for Applied Scientists and Engineers* (John Wiley & Sons, 2008).

[41] R. B. Karabalin, M. C. Cross, and M. L. Roukes, Physical Review B **79**, 165309 (2009).